









Understanding Cu incorporation in the $\text{Cu}_x\text{Hg}_{2-x}\text{GeTe}_4$ structure using resonant x-ray diffractionBen L. Levy-Wendt ^{1,*} Brenden R. Ortiz ^{4,†} Lídia C. Gomes ^{2,3,‡} Kevin H. Stone ¹ Donata Passarello ¹
Elif Ertekin ^{2,3,§} Eric S. Toberer ^{4,||} and Michael F. Toney ^{1,¶}¹SLAC National Accelerator Laboratory, Menlo Park, California 94025 USA²University of Illinois at Urbana-Champaign, Urbana, Illinois, 61820 USA³National Center for Supercomputing Applications, Urbana, Illinois 61801, USA⁴Colorado School of Mines, Golden, Colorado 80401, USA

(DMREF Collaboration)



(Received 7 October 2020; accepted 21 December 2020; published 15 January 2021)

The ability to control carrier concentration based on the extent of Cu solubility in the $\text{Cu}_x\text{Hg}_{2-x}\text{GeTe}_4$ alloy compound (where $0 \leq x \leq 1$) makes $\text{Cu}_x\text{Hg}_{2-x}\text{GeTe}_4$ an interesting case study in the field of thermoelectrics. While Cu clearly plays a role in this process, it is unknown exactly how Cu incorporates into the $\text{Cu}_x\text{Hg}_{2-x}\text{GeTe}_4$ crystal structure and how this affects the carrier concentration. In this work, we use a combination of resonant energy x-ray diffraction (REXD) experiments and density functional theory (DFT) calculations to elucidate the nature of Cu incorporation into the $\text{Cu}_x\text{Hg}_{2-x}\text{GeTe}_4$ structure. REXD across the Cu_k edge facilitates the characterization of Cu incorporation in the $\text{Cu}_x\text{Hg}_{2-x}\text{GeTe}_4$ alloy and enables direct quantification of antisite defects. We find that Cu substitutes for Hg at a 2:1 ratio, wherein Cu annihilates a vacancy and swaps with a Hg atom. DFT calculations confirm this result and further indicate that the incorporation of Cu occurs preferentially on one of the $z = 1/4$ or $z = 3/4$ planes before filling the other plane. Furthermore, the amount of Cu_{Hg} antisite defects quantified by REXD was found to be directly proportional to the experimentally measured hole concentration, indicating that the Cu_{Hg} defects are the driving force for tuning carrier concentration in the $\text{Cu}_x\text{Hg}_{2-x}\text{GeTe}_4$ alloy. The link uncovered here between crystal structure, or more specifically antisite defects, and carrier concentration can be extended to similar cation-disordered material systems and will aid the development of improved thermoelectric and other functional materials through defect engineering.

DOI: [10.1103/PhysRevMaterials.5.015402](https://doi.org/10.1103/PhysRevMaterials.5.015402)

I. INTRODUCTION

Cation-disordered semiconductors are an emerging class of materials with properties that are largely governed by lattice site disorder. Site disorder and occupancy are particularly important in optoelectronic and thermoelectric materials, where defect engineering can be utilized to design materials with improved properties such as carrier concentration or lattice thermal conductivity [1,2]. Further insight on how cation disorder can be utilized to control a material's properties depends on establishing detailed structure-function relationships. However, pinpointing the source of disorder within materials as well as quantifying the extent of disorder are experimentally challenging tasks.

Quantitative insight into structure-property relationships in cation-disordered materials is often missing from an experimental viewpoint due to the difficulty of characterizing small defect/dopant concentrations. Traditional methods of structural characterization, such as x-ray diffraction (XRD), are excellent for understanding a material's long-range order but are notoriously poor at quantifying small concentrations of defects and dopants. To address this deficiency, a variant of XRD—known as resonant energy x-ray diffraction (REXD)—takes advantage of the energy dependence of atomic scattering factors by measuring the intensity of Bragg peaks as a function of energy across an elemental absorption edge. The atomic scattering factor of a given element changes significantly near its respective absorption edge, which enables the ability to tune the scattering effects of a given element. The change in scattering power elucidates lattice site occupancies that are difficult to identify with traditional XRD, such as elements with similar atomic numbers occupying symmetric sites [3,4]. REXD can also be used to probe the presence of elements in small point defect quantities [5–7]. Here, we use REXD to examine cation site disorder in thermoelectric materials, which require a delicate optimization between low thermal conductivity and high charge carrier mobility.

* Also at Stanford University, Stanford, California 94305, USA.

† Also at University of California Santa Barbara, Santa Barbara, California 93106, USA.

‡ Also at Instituto de Física Teórica, São Paulo State University (UNESP), São Paulo, Brazil.

§ ertekin@illinois.edu

|| etoberer@mines.edu

¶ michael.toney@colorado.edu; he/him/his; Also at University of Colorado Boulder, Boulder, Colorado 80309, USA.

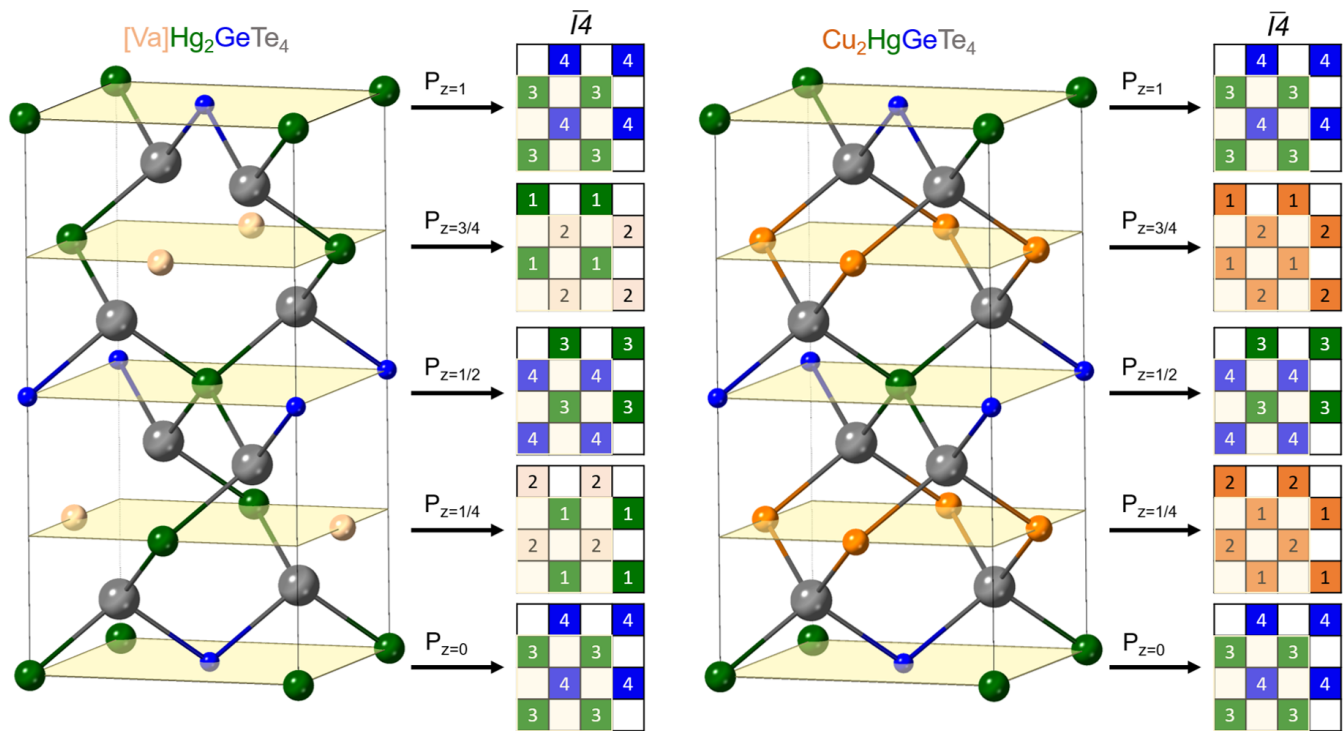


FIG. 1. The ternary endpoint, $[\text{Va}]\text{Hg}_2\text{GeTe}_4$, of the $\text{Cu}_{2x}\text{Hg}_{2-x}\text{GeTe}_4$ alloy crystallizes in the defect chalcopyrite structure and the quaternary endpoint, $\text{Cu}_2\text{HgGeTe}_4$, crystallizes in the stannite structure. The unit cell for these two compounds is shown here using the $I\bar{4}$ space group. The locations of specific atomic sites, as defined by the $I\bar{4}$ space group, are denoted numerically for each endpoint on the $z = 0, 1/4, 1/2, 3/4,$ and 1 planes and are colored based on the atom occupying that site for each composition—where vacancies are beige, Cu atoms are orange, Hg atoms are green, Ge atoms are blue, and Te atoms are gray. Each schematic plane represents a 2×2 unit cell, which is used later in DFT simulations, and the atoms contained in the original unit cell are highlighted within the yellow boxes on each plane.

One class of thermoelectric materials that demonstrates promise for achieving low thermal conductivity is the quaternary diamondlike semiconductors (DLS), such as $\text{Cu}_2(\text{IIB})(\text{IV})\text{Te}_4$ (IIB: Zn, Cd, Hg) (IV: Si, Ge, Sn) [8]. Among these compounds, $\text{Cu}_2\text{HgGeTe}_4$ was shown to exhibit unusually low thermal conductivity ($\kappa_L < 0.25$ W/mK) and high hole mobility ($\mu_0 > 50$ cm^2/Vs) [8]. The low thermal conductivity of $\text{Cu}_2\text{HgGeTe}_4$ was attributed to strong phonon scattering from Cu_{Hg} and Hg_{Cu} antisite defects, but further improvements in the overall efficiency of $\text{Cu}_2\text{HgGeTe}_4$ require an optimization of the carrier concentration.

Controlling carrier concentration in the DLS family of materials via manipulation of defects and dopants has been the topic of a number of previous studies [9–20]. Our previous work revealed the existence of a full solid solution between $\text{Cu}_2\text{HgGeTe}_4$ and Hg_2GeTe_4 , denoted here as $\text{Cu}_{2x}\text{Hg}_{2-x}\text{GeTe}_4$ (where $0 \leq x \leq 1$) [21]. We demonstrated that the extent of Cu integration in $\text{Cu}_{2x}\text{Hg}_{2-x}\text{GeTe}_4$ could be used to manipulate the carrier concentration, from degenerate ($>10^{21}$ $\text{h}^+ \text{cm}^{-3}$) in $\text{Cu}_2\text{HgGeTe}_4$ to intrinsic ($<10^{17}$ $\text{h}^+ \text{cm}^{-3}$) in Hg_2GeTe_4 [21]. Considering that the alloy remained charge balanced, the mechanism for varying the carrier concentration was unknown.

The structure of the endpoints of the $\text{Cu}_{2x}\text{Hg}_{2-x}\text{GeTe}_4$ alloy are known to be stannite ($I\bar{4}2m$) for $\text{Cu}_2\text{HgGeTe}_4$ [8] and

defect chalcopyrite ($I\bar{4}$) for Hg_2GeTe_4 [21]. Since the $I\bar{4}2m$ space group is a maximal subgroup of the $I\bar{4}$ space group, $I\bar{4}$ can be used to describe the structure of both $\text{Cu}_2\text{HgGeTe}_4$ and Hg_2GeTe_4 . The unit cell for these two endpoints of the $\text{Cu}_{2x}\text{Hg}_{2-x}\text{GeTe}_4$ alloy are shown in Fig. 1 along with a schematic that shows the location of each atomic site on the $z = 0, 1/4, 1/2, 3/4,$ and 1 planes (see Supplemental Material, Fig. 1, for unit cells of all compositions [22]). For the sake of clarity, Hg_2GeTe_4 is denoted as $[\text{Va}]\text{Hg}_2\text{GeTe}_4$ in Fig. 1 to emphasize the vacancy on site 2 for that structure.

In this work, we use a combination of REXD and density functional theory (DFT) calculations to characterize the $\text{Cu}_{2x}\text{Hg}_{2-x}\text{GeTe}_4$ crystal structure as a function of alloy composition. We find that vacancy ordering, where the vacancies prefer to occupy a single site, is maintained across all alloy compositions. Our DFT results indicate that Cu incorporates into the alloy structure by preferentially occupying sites 1 and 2 of the $z = 1/4$ plane equally before moving on to the $z = 3/4$ plane (see Fig. 1). Furthermore, we show that the extent of Cu_{Hg} antisite defects increases in direct proportionality with the experimentally measured hole concentrations. This work demonstrates how in-depth structural characterizations, including quantification of point defects, can provide valuable insight into how a material's structure affects electronic properties.

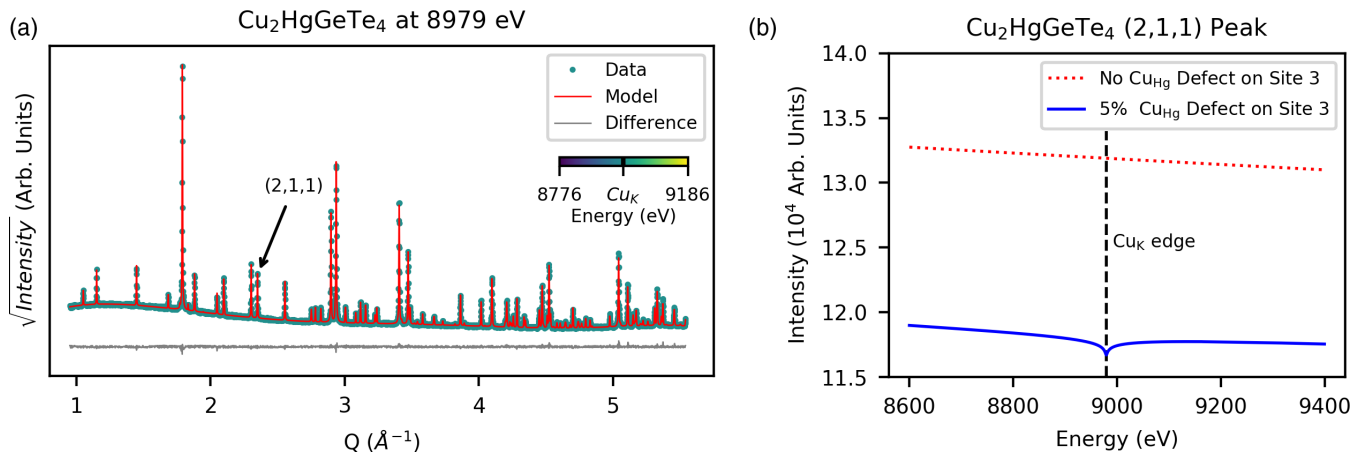


FIG. 2. (a) A sample REXD pattern collected for the sample at the Cu_K edge (8979 eV). The (2,1,1) peak is pointed out here with an arrow. (b) REXD simulations of the (2,1,1) peak for the quaternary sample demonstrating the difference between a sample with no antisite defects and a sample with 5% Cu_{Hg} antisite defects. The sample with 5% antisite defects demonstrates a sudden decrease in intensity across the Cu_K edge that is not present for the sample without antisite defects.

II. MATERIALS AND METHODS

1. Experimental

Powder samples of $\text{Cu}_{2x}\text{Hg}_{2-x}\text{GeTe}_4$ ($x = 0, 0.2, 0.4, 0.6, 0.8,$ and 1) from our previous study were also used here. We synthesized these via solid-state reaction as described previously [21]. All samples contain a trace amount of intentional impurities from the phase boundary mapping process [21] ($<1.80\%$ of HgTe and $<5.02\%$ of GeTe) as determined by our XRD phase fraction analysis.

High-resolution x-ray diffraction (HRXRD) experiments were conducted at beamline 11-BM of the Advanced Photon Source (APS) with a wavelength of 0.413 \AA . Data were collected by rotating the detector array of 12 independent point detectors (spaced apart by $\sim 2^\circ$) from 2° to 28° , thus covering an angular range from 2° to 50° , in increments of 0.001° at a scan speed of $0.01^\circ/\text{s}$. All samples were diluted with a 1:10 mol ratio of amorphous SiO_2 before being loaded into 0.5-mm glass capillaries (special glass, Charles Supper).

Resonant x-ray diffraction measurements were carried out at both beamline 2-1 of the Stanford Synchrotron Radiation Lightsource and beamline 33-BM of the APS. In both cases, samples were measured under Bragg-Brentano geometry using Si zero background plates and scattered x rays were detected using a Pilatus 100 K area detector. All samples were measured under an inert gas environment. Full powder diffraction patterns were measured across the Cu_K absorption edge for every sample. $\text{Cu}_{0.8}\text{Hg}_{1.6}\text{GeTe}_4$ was measured at 33-BM and all remaining Cu containing samples ($\text{Cu}_{2x}\text{Hg}_{2-x}\text{GeTe}_4$, where $x = 0.2, 0.6, 0.8,$ and 1) were measured at beamline 2-1. Samples measured at 2-1 were rocked by $\pm 0.5^\circ \text{C}$ during measurements to enhance powder averaging, but samples measured at 33-BM were not rocked.

All synchrotron diffraction data was analyzed using the TOPAS Academic software package and modeled to a unified structural model using Rietveld refinement. This structural model was based upon the lower symmetry Hg_2GeTe_4 compound, which has space group $I\bar{4}$. The lower degree of symmetry of this space group has the advantage that it enables

the use of a single structural model for all measured alloy compositions.

The first step in the analysis process was to perform Rietveld refinement on the HRXRD data. For each sample composition, the data were analyzed by refinement on lattice parameters, atomic occupancies, thermal parameters, and the atomic position of the Te atom in site 5. While the sites 1, 2, 3, and 4 atoms all lie on special positions within the unit cell, the atomic position of the Te atom in site 5 was refined as ($x, y,$ and z). Peak broadening was fit using a combination of Gaussian and Lorentzian contributions from size and microstrain parameters. Errors were obtained using the bootstrapping method with 25 iterations [23–25].

The results of the HRXRD refinement (see Supplemental Material, Figs. 2–7 [22]) were then used as the starting point for the REXD refinement. For a given sample composition, all the REXD patterns collected at different energies were corefined using a single structural model (see Supplemental Material, Example 1, for a sample input file [22]). All nonoccupancy parameters (i.e., thermal parameters, lattice parameters, and the Te atom position) were fixed to the values determined by HRXRD because the HRXRD scans contain data at a higher Q range, which is most important for refining these parameters. This allows us to focus on refining only the atomic occupancies in the REXD refinements. Peak broadening was again fit using a combination of Gaussian and Lorentzian contributions from size and strain parameters, but further corrections were needed due to anisotropic peak broadening. For this correction, we used the Stephen's tetragonal model [26]. The REXD refinement also required the use of a surface roughness correction to account for overcompaction of the powders in certain measurements ($x = 0.2, 0.6,$ and 0.8). For this correction, we used a macro developed by Suortti [27]. The total occupancy for each site was constrained such that it could not exceed one and quadratic penalties were used to constrain the overall composition to the nominal stoichiometric value.

An example of the final refinements is shown in Fig. 2(a) for the $\text{Cu}_2\text{HgGeTe}_4$ sample at the Cu_K edge (see

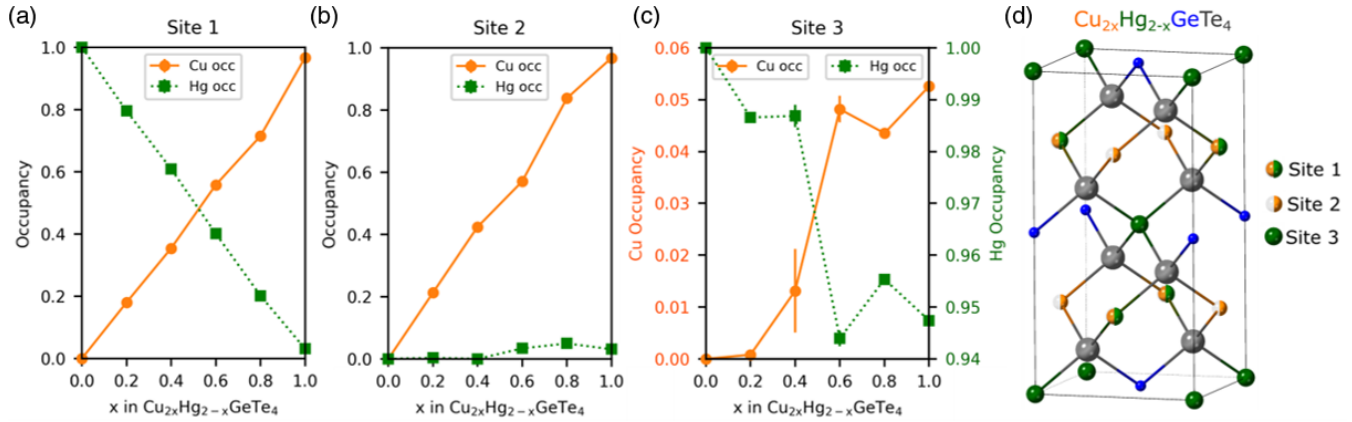


FIG. 3. (a–c) The Cu and Hg occupancies are plotted here for sites 1, 2, and 3. All occupancies were obtained via Rietveld refinement of REXD data on the $\text{Cu}_{2x}\text{Hg}_{2-x}\text{GeTe}_4$ alloys at room temperature. (d) An example unit cell for the $\text{Cu}_{2x}\text{Hg}_{2-x}\text{GeTe}_4$ alloy composition is shown here with sites 1, 2, and 3 indicated by the legend.

Supplemental Material, GIFs 1–5, for animations of the final REXD refinements of each composition as a function of energy [22]). The (2,1,1) peak is pointed out because it demonstrates the highest sensitivity to the presence of Cu_{Hg} defects, as indicated by the sudden drop in intensity across the Cu_k edge in Fig. 2(b). While modest, this change in intensity enables reliable quantification of antisite defects in our REXD refinements.

2. Computational

Investigation of the energetics of the alloys was performed using first-principles calculations within the DFT formalism [28,29]. The DFT calculations were performed with the plane-wave basis Vienna Ab initio Simulation Package (VASP) [30]. The generalized gradient approximation of Perdew-Burke-Ernzerhof [31] in the projector augmented wave formalism [32] was used. The Kohn-Sham orbitals were expanded using a plane-wave basis with a cutoff energy of 500 eV.

Total energies of Hg_2GeTe_4 and $\text{Cu}_2\text{HgGeTe}_4$ were computed using conventional cells composed of 14 and 16 atoms, respectively. In these cases, the Brillouin zone was sampled using a Γ -centered $8 \times 8 \times 4$ Monkhorst-Pack k -point grid [33].

The energy cost of the defects in the ternary, quaternary, and intermediate composition compounds were evaluated using a $2 \times 2 \times 1$ supercell (as shown schematically in Fig. 1) and a Γ -centered $4 \times 4 \times 4$ Monkhorst-Pack k -point grid. For the systems with intermediate composition, around 50 supercells with different site occupations were used. In this case, the supercells were generated with the Clusters Approach to Statistical Mechanics (CASM) open-source software package [34].

III. RESULTS AND DISCUSSION

To understand how Cu integrates into the $\text{Cu}_{2x}\text{Hg}_{2-x}\text{GeTe}_4$ structure, we use REXD across the Cu_k edge to probe the atomic occupancies of sites 1, 2, and 3 for each Cu-containing compound ($x = 0.2, 0.4, 0.6, 0.8,$ and 1). HRXRD was used for Hg_2GeTe_4 ($x = 0$) since this compound contains no Cu. These occupancies, plotted in Figs. 3(a)–3(c), provide insight

into how much of each type of atom lies on a specific lattice site (see Supplemental Material, Table 1, for a table of REXD results [22]). As indicated in Fig. 3(d), site 1 refers to the site that is nominally occupied by some combination of Hg and Cu depending on the sample composition, site 2 refers to the site that is vacant in Hg_2GeTe_4 and nominally occupied by Cu in $\text{Cu}_2\text{HgGeTe}_4$, and site 3 is nominally occupied by Hg for all compositions. REXD across the Cu_k edge enables more accurate quantification of Cu atomic occupancies than would be possible using nonresonant XRD due to the enhanced sensitivity from the Cu resonance effect. This enhanced sensitivity to Cu is particularly critical for probing Cu_{Hg} antisite defects on site 3.

From Figs. 3(a)–3(b) at $x = 0$, it is apparent that site 1 is initially fully occupied by Hg and site 2 is completely vacant, indicating that there is ordering of the vacancies and Hg atoms between sites 1 and 2 on the $z = 1/4$ and $z = 3/4$ planes in Hg_2GeTe_4 . If Hg exists in Hg_2GeTe_4 in the Hg^{2+} state and Cu integrates into the alloy as Cu^{1+} , then it follows that charge balance is maintained by exchanging Cu and Hg in a 2:1 ratio as the alloy progresses from Hg_2GeTe_4 ($x = 0$) to $\text{Cu}_2\text{HgGeTe}_4$ ($x = 1$).

Examining the occupancies of sites 1 and 2 in Figs. 3(a) and 3(b), respectively, reveal that Cu fills these two sites roughly equally as the alloy composition changes from $x = 0$ to $x = 1$. Furthermore, the amount of additional Cu introduced into the alloy in sites 1 and 2 at each sequential composition is consistently twice the amount of Hg that is removed from site 1. Taken together, these results indicate that Cu fills the $\text{Cu}_{2x}\text{Hg}_{2-x}\text{GeTe}_4$ lattice in a 2:1 ratio with Hg wherein one Cu atom annihilates a Hg vacancy on site 2 while another Cu atom swaps with an existing Hg atom on site 1.

Meanwhile, Hg continues to prefer occupying site 1 rather than site 2 for all compositions—as evidenced by significantly higher occupancies of Hg on site 1 in Fig. 3(a) than on site 2 in Fig. 3(b)—except for $\text{Cu}_2\text{HgGeTe}_4$, where there is very little Hg on either site. However, there is a slight increase in the Hg occupancy of site 2 above the vacancy levels for the $x = 0.6, 0.8,$ and 1 compositions in Fig. 3(b), which points to the possibility of Cu_{Hg} antisite defects in the alloy system.

To further understand the possible source of these defects, the occupancy of site 3 is plotted in Fig. 3(c) where we see that the Hg occupancy decreases and is accompanied by a simultaneous increase in the Cu site 3 occupancy as the alloy approaches the $x = 1$ composition. The presence of Cu on site 3 demonstrates the presence of Cu_{Hg} antisite defects. The amount of these defects increases as the alloy composition moves closer to $x = 1$ ($\text{Cu}_2\text{HgGeTe}_4$). The propensity for $\text{Cu}_2\text{HgGeTe}_4$ to demonstrate Cu_{Hg} swaps and for Hg_2GeTe_4 to be strongly ordered (i.e., no Hg_{Va} swaps) is confirmed by DFT calculations, which reveal that the energy cost ΔE for Cu_{Hg} swaps in $\text{Cu}_2\text{HgGeTe}_4$ ($\Delta E = 0.23$ eV) is about three times smaller than for Hg_{Va} swaps in Hg_2GeTe_4 ($\Delta E = 0.67 - 0.76$ eV).

In brief summary, REXD experiments have revealed that Cu integrates into the $\text{Cu}_{2x}\text{Hg}_{2-x}\text{GeTe}_4$ alloy structure in a 2:1 ratio with Hg where Cu simultaneously swaps with a Hg atom on site 1 and annihilates a vacancy on site 2. We also know that Hg-vacancy ordering is strongest at compositions closest to $x = 0$ (Hg_2GeTe_4) and that there is an increasing likelihood of Cu_{Hg} antisite defects on site 3 as Cu incorporates into the alloy composition. However, REXD experiments are still unable to tell us whether the Cu integration occurs primarily on one of the $z = 1/4$ or $z = 3/4$ planes or on both simultaneously. This leaves three possible scenarios for how Cu integrates into the $\text{Cu}_{2x}\text{Hg}_{2-x}\text{GeTe}_4$ structure. These three scenarios are illustrated in Fig. 4(b) for the intermediate $x = 0.5$ alloy composition ($\text{CuHg}_{1.5}\text{GeTe}_4$) and are described as follows: scenario 1, Cu occupies site 1 on one plane and site 2 on the other plane; scenario 2, Cu occupies sites 1 and 2 on both planes equally; and scenario 3, Cu occupies sites 1 and 2 exclusively on one plane. Due to site symmetry, we are unable to differentiate between these three possible scenarios using REXD, so we turn to DFT calculations performed on the intermediate composition ($x = 0.5$) to see what the preferred structure is on the basis of total energy. Figure 4(a) shows the total energy in meV/atom for approximately 50 potential configurations of the $x = 0.5$ alloy. The three configurations highlighted in green, blue, and red show the lowest energy permutation of each of the three scenarios described previously. Of these, scenario 3 has the lowest energy, indicating that Cu prefers to fill one plane entirely before beginning to fill the other plane as Cu is incorporated into the $\text{Cu}_{2x}\text{Hg}_{2-x}\text{GeTe}_4$ structure. Under scenario 3, the intermediate $x = 0.5$ alloy composition ($\text{CuHg}_{1.5}\text{GeTe}_4$) can be expressed using the space group $P\bar{4}$, which is provided in the Supplemental Material, Example 2 [22].

One possible explanation for why scenario 3 is lower in energy than the other scenarios is based on electrostatics. In Fig. 4(b), the Te atoms that sit above and below the $z = 1/4$ and $z = 3/4$ planes are shown in light gray and dark gray circles, respectively. Looking at the Hg_2GeTe_4 and $\text{Cu}_2\text{HgGeTe}_4$ unit cells in Fig. 1, we see that each Te atom is bonded to one Ge atom and at least one Hg atom (for instance, from the $z = 0$ or $z = 1/2$ planes) regardless of composition. Assuming Ge has an oxidation state of 4^+ and Hg has an oxidation state of 2^+ , then each Te atom needs to be surrounded by an additional charge of 2^+ (in the $z = 1/4$ and $3/4$ planes) in order for the octet rule to be satisfied. This is accomplished in $\text{Cu}_2\text{HgGeTe}_4$ by two Cu^{1+} atoms and in Hg_2GeTe_4 by one Hg^{2+} atom

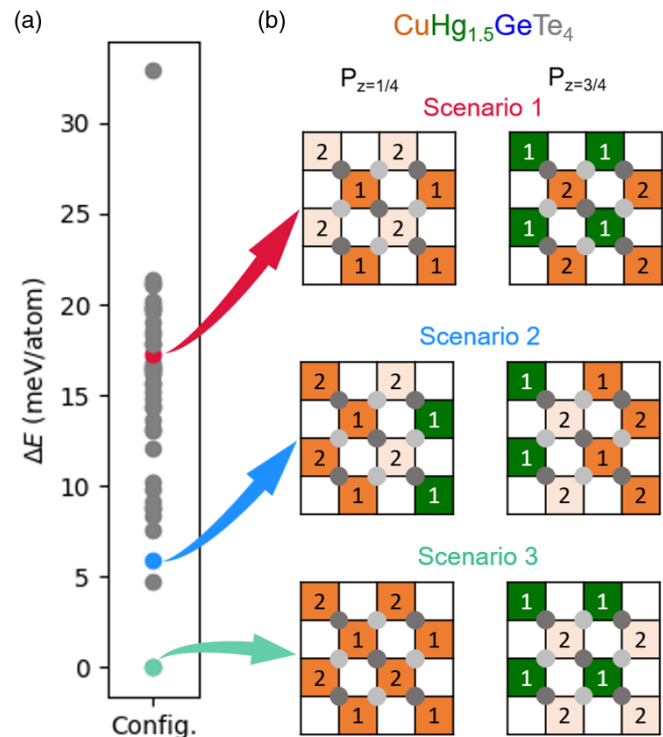


FIG. 4. (a) DFT total energies for approximately 50 permutations (gray dots) of the intermediate $\text{CuHg}_{1.5}\text{GeTe}_4$ alloy. The energies are referenced to the lowest energy configuration, shown by the light-green dot. (b) The lowest energy permutation of each of the three possible scenarios from REXD results is demonstrated schematically. Scenario 3, where Cu occupies sites 1 and 2 exclusively on the $z = 1/4$ plane, has the lowest energy and is therefore the most favorable. Te atoms that sit above and below the $z = 1/4$ and $3/4$ planes are shown in light gray and dark gray circles, respectively.

and a vacancy. Similarly, for the intermediate compositions in Fig. 4(b), the octet rule will be satisfied whenever the gray dots representing Te atoms are between two atoms, or boxes, for which the net charge is 2^+ . Since Cu (orange box) has an oxidation state of 1^+ , Hg (green box) has an oxidation state of 2^+ and vacancies (beige box) have no charge, scenario 3 is the only scenario that satisfies the octet rule for all Te atoms. This argument is supported by the observation that in scenario 1 none of the Te atoms satisfy the octet rule and scenario 1 has the highest energy. The discussion up to this point has provided a detailed understanding of how Cu is integrated into the $\text{Cu}_{2x}\text{Hg}_{2-x}\text{GeTe}_4$ structure, so we now turn our attention to how this structure affects the thermoelectric properties. Converting the site 3 Cu occupancies from Fig. 3 into Cu_{Hg} concentrations (as explained in the Supplemental Material, Eq. (1) [22]) revealed a direct proportionality with previously measured hole concentrations [21] across the alloy composition range, as shown in Fig. 5. This suggests that Cu_{Hg} antisite defects, which are the source of Cu on site 3, are responsible for tuning the carrier concentration in the $\text{Cu}_{2x}\text{Hg}_{2-x}\text{GeTe}_4$ alloys.

The ability to tune carrier concentration via manipulation of antisite defects is a striking result worth further consideration. While it is intuitive that Cu_{Hg} antisite defects might

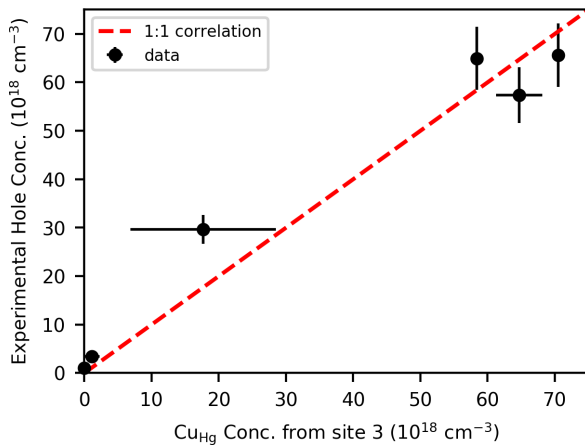


FIG. 5. The experimentally measured hole concentration, taken from Ref. [21] (with a standard error of 10%), is plotted here as a function of the site 3 Cu_{Hg} concentration from the current study. A line with a slope of 1 is also drawn to illustrate the strong correlation, which indicates that Cu_{Hg} antisite defects are responsible for controlling the carrier concentration of $\text{Cu}_{2x}\text{Hg}_{2-x}\text{GeTe}_4$ alloys.

increase as the alloy composition becomes more Cu rich, it was unexpected to see that the correlation between the site 3 Cu concentration and the experimentally measured hole concentrations was directly proportional (e.g., 1:1) because this implies that no other defects contribute to the carrier concentration. In particular, we expected that Cu vacancies (V_{Cu}) may also contribute to the carrier concentration via hole generation. However, two key facts justify our implicit disregard for V_{Cu} here. First is that DFT defect diagrams for the Cu-rich $\text{Cu}_2\text{HgGeTe}_4$ compound predict Cu_{Hg} as the dominant defect [35]. Second is that if V_{Cu} were responsible for the increased carrier concentration in the $\text{Cu}_{2x}\text{Hg}_{2-x}\text{GeTe}_4$ alloy, then we would expect to see a decrease in the carrier concentration as excess Cu is incorporated into $\text{Cu}_2\text{HgGeTe}_4$ because this excess Cu would annihilate V_{Cu} . However, our previous work demonstrated that integrating excess Cu into $\text{Cu}_2\text{HgGeTe}_4$ actually led to a higher hole concentration [21], indicating that Cu_{Hg} —not V_{Cu} —is the predominant defect in the alloy system. This work therefore demonstrates that Cu_{Hg} is a favorable defect and singularly determines the carrier concentration along the entire alloying series. Thus, these results justify our previous observations and demonstrate how REXD can provide immense insight into the defects of complex materials.

Looking beyond carrier concentration, our future work will focus on understanding the effect of Cu_{Hg} antisite defects on thermal conductivity using inelastic neutron scattering to ac-

quire phonon density of states spectra of the same compounds used in this study.

IV. CONCLUSION

We have shown through a combination of REXD experiments and DFT calculations that Cu integrates into the $\text{Cu}_{2x}\text{Hg}_{2-x}\text{GeTe}_4$ alloy compound in a 2:1 ratio with Hg where Cu simultaneously annihilates a vacancy and swaps with a Hg atom on the $z = 1/4$ and $z = 3/4$ planes. Furthermore, we showed that the ordering of vacancies is maintained as Cu is incorporated into the structure and that Cu atoms are likely to fill a single plane entirely before moving on to the next one. The presence of Cu_{Hg} antisite defects was quantified by REXD and shown to directly control the measured hole concentrations. These results indicate a systematic and ordered incorporation of Cu into $\text{Cu}_{2x}\text{Hg}_{2-x}\text{GeTe}_4$ rather than a randomized entropic process, which explains the linear nature of the effect of Cu incorporation on carrier concentration. The ability of REXD to both quantify the presence of antisite defects and understand how these defects affect the carrier concentration can have a significant impact on the development of future thermoelectric materials and semiconductors.

ACKNOWLEDGMENTS

B.L.L.-W, B.R.O, E.S.T., and M.F.T acknowledge support from the National Science Foundation, DMREF No. 1729594. L.C.G. and E.E acknowledge support from the National Science Foundation, DMREF No. 1729149. B.L.L.-W. acknowledges support from the National Science Foundation Graduate Research Fellowship under Grant No. DGE-114747. Use of the Stanford Synchrotron Radiation Lightsources, SLAC National Accelerator Laboratory, is supported by the DOE Office of Science (SC), Basic Energy Sciences (BES), under Contract No. DE-AC02-76SF00515. Use of the Advanced Photon Source was supported by the US Department of Energy, Office of Science, Office of Basic Energy Sciences, under Contract No. DE-AC02-06CH11357. We thank Saul Lapidus and Jenia Karapetrova for their support at APS beamlines 11-BM and 33-BM, respectively. Computational resources were provided by the Blue Waters sustained-petascale computing project, which is supported by the National Science Foundation (Grants No. OCI-0725070 and No. ACI-1238993), the State of Illinois, and, as of December, 2019, the National Geospatial-Intelligence Agency. Blue Waters is a joint effort of the University of Illinois at Urbana-Champaign and its National Center for Supercomputing Applications.

- [1] R. R. Schnepf, J. J. Cordell, M. B. Tellekamp, C. L. Melamed, A. L. Greenaway, A. Mis, G. L. Brennecke, S. Christensen, G. J. Tucker, E. S. Toberer, S. Lany, and A. C. Tamboli, Utilizing site disorder in the development of new energy-relevant semiconductors, *ACS Energy Lett.* **5**, 2027 (2020).
- [2] J. Pan, J. J. Cordell, G. J. Tucker, A. Zakutayev, A. C. Tamboli, and S. Lany, Perfect short-range ordered alloy with

line-compound-like properties in the $\text{ZnSnN}_2 : \text{ZnO}$ system, *npj Comput. Mater.* **6**, 63 (2020).

- [3] R. R. Schnepf, B. L. Levy-Wendt, M. B. Tellekamp, B. R. Ortiz, C. L. Melamed, L. T. Schelhas, K. H. Stone, M. F. Toney, E. S. Toberer, and A. C. Tamboli, Using resonant energy x-ray diffraction to extract chemical order parameters in ternary semiconductors, *J. Mater. Chem. C* **8**, 4350 (2020).

- [4] M. Christensen, N. Lock, J. Overgaard, and B. B. Iversen, Crystal structures of thermoelectric *n*- and *p*-type $\text{Ba}_8\text{Ga}_{16}\text{Ge}_{30}$ studied by single crystal, multitemperature, neutron diffraction, conventional x-ray diffraction and resonant synchrotron x-ray diffraction, *J. Am. Chem. Soc.* **128**, 15657 (2006).
- [5] K. H. Stone, S. T. Christensen, S. P. Harvey, G. Teeter, I. L. Repins, and M. F. Toney, Quantifying point defects in $\text{Cu}_2\text{ZnSn}(\text{S}, \text{Se})_4$ thin films using resonant x-ray diffraction, *Appl. Phys. Lett.* **109**, 161901 (2016).
- [6] L. T. Schelhas, K. H. Stone, S. P. Harvey, D. Zakhidov, A. Salleo, G. Teeter, I. L. Repins, and M. F. Toney, Point defects in $\text{Cu}_2\text{ZnSnSe}_4$ (CZTSe): Resonant x-ray diffraction study of the low-temperature order/disorder transition, *Phys. Status Solidi B* **254**, 1700156 (2017).
- [7] V. E. Dmitrienko and E. N. Ovchinnikova, Resonant X-ray diffraction: 'forbidden' Bragg reflections induced by thermal vibrations and point defects, *Acta Crystallogr. Sect. A* **56**, 340 (2000).
- [8] B. R. Ortiz, W. Peng, L. C. Gomes, P. Gorai, T. Zhu, D. M. Smiadak, G. J. Snyder, V. Stevanovic, E. Ertekin, A. Zevkink, and E. S. Toberer, Ultralow thermal conductivity in diamond-like semiconductors: Selective scattering of phonons from antisite defects, *Chem. Mater.* **30**, 3395 (2018).
- [9] Y.-T. Hsieh, Q. Han, C. Jiang, T.-B. Song, H. Chen, L. Meng, H. Zhou, and Y. Yang, Efficiency enhancement of $\text{Cu}_2\text{ZnSn}(\text{S}, \text{Se})_4$ solar cells via alkali metals doping, *Adv. Energy Mater.* **6**, 1502386 (2016).
- [10] N. Cheng, R. Liu, S. Bai, X. Shi, and L. Chen, Enhanced thermoelectric performance in Cd doped CuInTe_2 compounds, *J. Appl. Phys.* **115**, 163705 (2014).
- [11] A. Kosuga, R. Higashine, T. Plirdpring, M. Matsuzawa, K. Kurosaki, and S. Yamanaka, Effects of the defects on the thermoelectric properties of Cu–In–Te chalcopyrite-related compounds, *Jpn. J. Appl. Phys.* **51**, 121803 (2012).
- [12] A. Kosuga, T. Plirdpring, R. Higashine, M. Matsuzawa, K. Kurosaki, and S. Yamanaka, High-temperature thermoelectric properties of $\text{Cu}_{1-x}\text{InTe}_2$ with a chalcopyrite structure, *Appl. Phys. Lett.* **100**, 042108 (2012).
- [13] A. Yusufu, K. Kurosaki, A. Kosuga, T. Sugahara, Y. Ohishi, H. Muta, and S. Yamanaka, Thermoelectric properties of $\text{Ag}_{1-x}\text{GaTe}_2$ with chalcopyrite structure, *Appl. Phys. Lett.* **99**, 061902 (2011).
- [14] H. Xie, X. Su, G. Zheng, T. Zhu, K. Yin, Y. Yan, C. Uher, M. G. Kanatzidis, and X. Tang, The role of Zn in chalcopyrite CuFeS_2 : Enhanced thermoelectric properties of $\text{Cu}_{1-x}\text{Zn}_x\text{FeS}_2$ with in situ nanoprecipitates, *Adv. Energy Mater.* **7**, 1601299 (2017).
- [15] Y. Li, T. Zhang, Y. Qin, T. Day, G. Jeffrey Snyder, X. Shi, and L. Chen, Thermoelectric transport properties of diamond-like $\text{Cu}_{1-x}\text{Fe}_{1+x}\text{S}_2$ tetrahedral compounds, *J. Appl. Phys.* **116**, 203705 (2014).
- [16] D. Zhang, J. Yang, Q. Jiang, Z. Zhou, X. Li, J. Xin, A. Basit, Y. Ren, and X. He, Multi-cations compound $\text{Cu}_2\text{CoSnS}_4$: DFT calculating, band engineering and thermoelectric performance regulation, *Nano Energy* **36**, 156 (2017).
- [17] Y. Zhou, Q. Chen, L. Dong, and Y. Yin, Improving thermoelectric performance of chalcogenide $\text{Cu}_{2-2x}\text{CdSnSe}_4$ by Cu vacancy, *Nanosci. Nanotechnol. Lett.* **9**, 1520 (2017).
- [18] R. Chetty, A. Bali, and R. C. Mallik, Thermoelectric properties of indium doped $\text{Cu}_2\text{CdSnSe}_4$, *Intermetallics* **72**, 17 (2016).
- [19] M.-L. Liu, I.-W. Chen, F.-Q. Huang, and L.-D. Chen, Improved thermoelectric properties of Cu-doped quaternary chalcogenides of $\text{Cu}_2\text{CdSnSe}_4$, *Adv. Mater.* **21**, 3808 (2009).
- [20] X. Y. Shi, F. Q. Huang, M. L. Liu, and L. D. Chen, Thermoelectric properties of tetrahedrally bonded wide-gap stannite compounds $\text{Cu}_2\text{ZnSn}_{1-x}\text{In}_x\text{Se}_4$, *Appl. Phys. Lett.* **94**, 122103 (2009).
- [21] B. R. Ortiz, K. Gordiz, L. C. Gomes, T. Braden, J. M. Adamczyk, J. Qu, E. Ertekin, and E. S. Toberer, Carrier density control in $\text{Cu}_2\text{HgGeTe}_4$ and discovery of Hg_2GeTe_4 via phase boundary mapping, *J. Mater. Chem. A* **7**, 621 (2019).
- [22] See Supplemental Material at <http://link.aps.org/supplemental/10.1103/PhysRevMaterials.5.015402> for $\text{Cu}_{2-x}\text{Hg}_{2-x}\text{GeTe}_4$ unit cells, HRXRD spectra, tabulated REXD results, an equation for Cu_{Hg} concentration, an example TOPAS-Academic input file, a CIF file for $\text{CuHg}_{1.5}\text{GeTe}_4$, and GIFs illustrating the REXD refinements.
- [23] B. Efron and R. Tibshirani, Bootstrap methods for standard errors, confidence intervals, and other measures of statistical accuracy, *Stat. Sci.* **1**, 54 (1986).
- [24] T. J. DiCiccio and B. Efron, Bootstrap confidence intervals, *Stat. Sci.* **11**, 189 (1996).
- [25] M. R. Chernick, *Bootstrap Methods: A Guide for Practitioners and Researchers*, 2nd ed. (Wiley & Sons, New York, 2007).
- [26] P. W. Stephens, Phenomenological model of anisotropic peak broadening in powder diffraction, *J. Appl. Crystallogr.* **32**, 281 (1999).
- [27] P. Suortti, Effects of porosity and surface roughness on the X-ray intensity reflected from a powder specimen, *J. Appl. Crystallogr.* **5**, 325 (1972).
- [28] P. Hohenberg and W. Kohn, Inhomogeneous electron gas, *Phys. Rev.* **136**, B864 (1964).
- [29] W. Kohn and L. J. Sham, Self-consistent equations including exchange and correlation effects, *Phys. Rev.* **140**, A1133 (1965).
- [30] G. Kresse and J. Furthmüller, Efficient iterative schemes for *ab initio* total-energy calculations using a plane-wave basis set, *Phys. Rev. B* **54**, 11169 (1996).
- [31] J. P. Perdew, K. Burke, and M. Ernzerhof, Generalized Gradient Approximation Made Simple, *Phys. Rev. Lett.* **77**, 3865 (1996).
- [32] P. E. Blöchl, Projector augmented-wave method, *Phys. Rev. B* **50**, 17953 (1994).
- [33] H. J. Monkhorst and J. D. Pack, Special points for Brillouin-zone integrations, *Phys. Rev. B* **13**, 5188 (1976).
- [34] CASM, v0.2.1 (2017). Available from <https://github.com/prisms-center/CASMcode>, doi: 10.5281/zenodo.546148.
- [35] J. Qu, L. C. Gomes, J. M. Adamczyk, E. S. Toberer, and E. Ertekin, Dopability and carrier density control for thermoelectric applications (unpublished).